Scattering and transport properties of the three classical Wigner-Dyson ensembles at the Anderson transition

A. M. Martínez-Argüello [1], M. Carrera-Núñez [2,*] and J. A. Méndez-Bermúdez [1]

[1]*Instituto de Física, Benemérita Universidad Autónoma de Puebla, Apartado Postal J-48, 72570 Puebla, Puebla, Mexico*
[2]*Departamento de Ciencias Naturales y Exactas, Universidad de Guadalajara,*
Carretera Guadalajara–Ameca Km. 45.5 C.P. 46600. Ameca, Jalisco, Mexico

An extensive numerical analysis of the scattering and transport properties of the power-law banded random matrix model (PBRM) at criticality in the presence of orthogonal, unitary, and symplectic symmetries is presented. Our results show a good agreement with existing analytical expressions in the metallic regime and with heuristic relations widely used in studies of the PBRM model in the presence of orthogonal and unitary symmetries. Moreover, our results confirm that the multifractal behavior of disordered systems at criticality can be probed by measuring scattering and transport properties, which is of paramount importance from the experimental point of view. Thus, a full picture of the scattering and transport properties of the PBRM model at criticality corresponding to the three classical Wigner-Dyson ensembles is provided.

I. INTRODUCTION

Scattering and transport properties of disordered mesoscopic conductors have been of interest for a long time (see Refs. [1–3] and the references therein). Among the diverse phenomena observed in these systems, the disorder-induced localization-delocalization transition of electronic states, known as Anderson or metal-insulator transition (MIT), has received special attention [1,4–8]. At the MIT, the energy spectra show anomalous behavior while the electronic states present multifractal characteristics and strong amplitude fluctuations. The latter are usually described by an infinite set of critical exponents and represent one of the most important characteristics of the MIT [4,6,9–19]. At criticality, i.e., at the MIT, both the dimensionality and the symmetries present in the system play an important role.

The statistical properties of ordinary disordered samples are well described by the random matrix theory (RMT) [20] for which three universal symmetry classes are known: the orthogonal [the symplectic] class describing systems in the presence of time reversal and presence [absence] of spin-rotation symmetry and the unitary class for systems with broken time-reversal symmetry. In the Dyson scheme these symmetries are labeled by the indices $\beta = 1, 2$, and 4, for the orthogonal, the unitary, and the symplectic classes, respectively [21–23].

Until now, many important features of disordered systems at the MIT have been analyzed using numerical techniques. This is due to the complexity in obtaining analytical expressions at criticality, some of which are available only perturbatively. In particular, the so-called power-law banded random matrix (PBRM) model has widely been used since it captures all the key features of the Anderson critical point and

is also convenient for its low computational cost [6,24–26]. For the closed system, on the one hand, since the appearance of the PBRM model originally proposed by Mirlin *et al.* [24], a plethora of studies regarding different aspects of the model with $\beta = 1$ symmetry have been performed [6,11,24,26–35] while less studies regarding $\beta = 2$ symmetry are reported [11,32,33,36]. Moreover, the energy spectra and multifractal behavior of the PBRM model in the presence of the symplectic symmetry ($\beta = 4$) have recently been analyzed [37]. For the open system, on the other hand, several scattering and transport properties of the model when the system is in the presence of time-reversal invariance ($\beta = 1$) [32,38–42], which are in agreement with the ones obtained by using the three-dimensional Anderson model at MIT [28,41], have been investigated. However, to our knowledge, the analysis of the scattering and transport properties of the PBRM model for the unitary case are scarce [43] while the symplectic case has been left unexplored.

It is the purpose of the present paper to deepening the understanding of the scattering and transport properties of critical systems belonging to the symplectic class; that is, we study the open symplectic PBRM ensemble at criticality. The regime of a small number of single-mode leads attached to the PBRM model is studied in detail. Nevertheless, the multichannel or multiple single-mode leads setup is also studied for some scattering and transport quantities of interest. In order to provide a full picture of the PBRM model for the three classical Wigner-Dyson ensembles, the scattering and transport properties of the PBRM model for the $\beta = 1$ and $\beta = 2$ cases, previously considered in the literature, are also reviewed and extended when appropriate. Our results are also compared with RMT predictions in the appropriate limits.

The organization of the paper is as follows. In the next section, the generalized PBRM model in the presence of the three symmetry classes and the scattering setup are described. The perfect coupling regime, the Wigner delay time, and the

---
*moises.carrera.n@gmail.com

resonance widths when the PBRM supports one open channel are analyzed in detail in Sec. III. This is of particular interest, since it shows that the multifractal properties of the isolated PBRM model can be probed by measuring transport properties. The analysis of the scattering and transport properties of the PBRM model in the two and four open-channel setups is the subject of Sec. IV. In the same section, the scattering and transport properties in the multichannel setup are also presented. Finally, the conclusions are given in Sec. V.

II. MODEL AND SCATTERING SETUP

The PBRM model describes one-dimensional (1D) tight-binding wires of length N with random long-range hoppings [6,24]. In the presence of the three symmetry classes, it is represented by $N \times N$ real symmetric ($\beta = 1$), complex Hermitian ($\beta = 2$), or $2N \times 2N$ quaternion-real Hermitian ($\beta = 4$) matrices whose elements are statistically independent random variables drawn from a normal distribution with zero mean and variance given by [37]

$$\langle |H_{ii}|^2 \rangle = \beta^{-1} \quad \text{and}$$

$$\langle |H_{ij}|^2 \rangle = \frac{1}{2(1+\delta_{\beta,4})} \frac{1}{1 + \left[\sin\left(\frac{\pi|i-j|}{N}\right) \middle/ \left(\frac{\pi b}{N}\right) \right]^{2\mu}}. \quad (1)$$

The matrix sizes are $L = N$ for $\beta = 1$ and 2 and $L = 2N$ for $\beta = 4$. The PBRM model is a random matrix ensemble with off-diagonal matrix elements decaying away from the diagonal in a power-law fashion. Also, in (1) the PBRM model is in its periodic version, i.e., the 1D wire is in a ring geometry, where μ and b are the parameters of the model and $\delta_{\beta,4}$ is the Kronecker delta. In particular, for the symplectic case ($\beta = 4$) the PBRM model preserves the quaternion structure of the Hamiltonian where each eigenvalue is twofold degenerate due to Kramers degeneracy (for more details see Ref. [37]). The power-law decay $\mu = 1$ sets the PBRM model at the MIT critical point [6,11,24,26,28–31,37]. Furthermore, regardless of the value of μ, insulating- to metallic-like behavior may be induced by varying the effective bandwidth b from small b to large b values, respectively. Here the scattering and transport properties of the PBRM model of Eq. (1) at criticality, $\mu = 1$, is the focus of this work.

The isolated wire is opened by attaching to it M semi-infinite single-channel leads, each one described by a 1D tight-binding Hamiltonian,

$$H_{\text{lead}} = \sum_{n=1}^{-\infty} (|n\rangle\langle n+1| + |n+1\rangle\langle n|), \quad (2)$$

thus M establishes the number of open channels or propagating modes. The $M \times M$ scattering matrix, $S(E)$, can be written as [42,44–46]

$$S(E) = \begin{pmatrix} r & t' \\ t & r' \end{pmatrix} = \mathbb{1}_M - 2i\pi W^T (E \mathbb{1}_L - H_{\text{eff}})^{-1} W, \quad (3)$$

where r [r'] and t [t'] are the reflection and transmission amplitudes when the incidence is from the left [right], $\mathbb{1}_n$ stands for the unit matrix of dimension n, E is the energy, and the superscript T indicates the matrix transposition operation. In Eq. (3), H_{eff} is the non-Hermitian effective Hamiltonian given

by

$$H_{\text{eff}} = H - i\pi W W^T, \quad (4)$$

where H is the $L \times L$ Hamiltonian matrix of the PBRM model that describes the isolated wire with L resonant states and W is an $L \times M$ energy independent matrix that couples those resonant states to the M propagating modes in the leads. The elements of W are $W_{ij} = w_0 \delta_{ij_0}$, where w_0 is the coupling strength between the wire and the leads and $j_0 = 1, \ldots, M$ are the sites at which the leads are attached. According to the symmetry present in the Hamiltonian, the S matrix is unitary symmetric, unitary, and unitary self-dual matrix for $\beta = 1, 2$, and 4, respectively [2]. Additionally, due to the ring geometry of the isolated wire under consideration, the scattering and transport properties do not depend on which site the leads are attached to. Then, for simplicity and without loss of generality, in this work the leads are attached at consecutive sites of the wire.

III. PBRM MODEL WITH ONE OPEN CHANNEL

In this section, the statistical properties of scattering phases, Wigner delay time, and resonance widths, when the scattering system supports one open channel and is in the presence of the $\beta = 1, 2$, and 4 symmetries are analyzed. The relation between Wigner delay times and the properties of the spectra and eigenstates of the corresponding isolated wire are also discussed.

A. Perfect coupling regime

In the one-channel setup, the scattering matrix of Eq. (3) reduces to a phase given by $S(E) = e^{i\Phi(E)}$. This case corresponds to a single-channel lead attached to the wire (1). For the PBRM model in the limit $b \gg 1$ (metallic-like regime), that phase is distributed according to the following expression [47]:

$$\mathcal{P}(\Phi) = \frac{1}{2\pi} \frac{1}{\gamma + \sqrt{\gamma^2 - 1}\cos\Phi}, \quad (5)$$

where $\gamma = (1 + |\langle S \rangle|^2)/(1 - |\langle S \rangle|^2)$. In the so-called *perfect coupling regime*, the averaged scattering matrix $\langle S \rangle$, also known as optical matrix, vanishes and the phase is uniformly distributed over the unit circle.

Before proceeding with the analysis of the phase distribution (5), some general statements about the numerical simulations are given. For the statistical analysis shown throughout this work, most calculations are performed in the perfect coupling regime since in this limit a number of analytical predictions from RMT are known. Also, the calculations are performed around $E \sim 0$ considering wire lengths of $N = 50, 100, 200, 400$, and 800 with $10^6, 10^6, 10^5, 10^5$, and 10^5 random realizations, respectively. All fittings are performed through the nonlinear least-squares Marquardt-Levenberg algorithm as implemented by gnuplot. The error bars are computed by the jackknife method, unless specified otherwise. Histograms for the probability distributions and for the cumulative probabilities do not contain error bars since the statistics is done with a large amount of data such that the error is not significant.
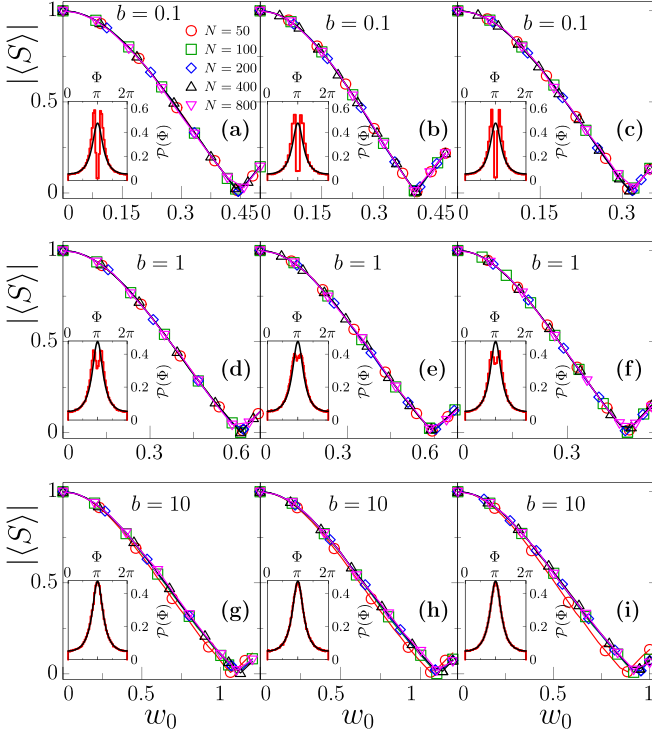
FIG. 1. Absolute value of the optical S matrix for the PBRM model at criticality as a function of the coupling strength, w_0, for values of b indicated in each panel and several wire lengths N as indicated in panel (a). The symmetries are $\beta = 1$ (first column), 2 (second column), and 4 (third column). The insets show numerically obtained histograms (red lines) compared with the phase distribution (5) (black continuous lines) for $|\langle S \rangle| = 0.5$. The error bars are smaller than the symbol size, so they are not displayed.

In Fig. 1, the modulus of the optical matrix as a function of the coupling strength w_0 for the PBRM model at criticality with $\beta = 1$ (first column), $\beta = 2$ (second column), and $\beta = 4$ (third column) is shown. Different values of the bandwidth b and wire lengths N are considered. It is observed that the perfect coupling, $|\langle S \rangle| \approx 0$, does not depend on the wire length but shows a strong dependence on b. The perfect coupling is attained for values of $w_0 < 0.5$, $0.45 < w_0 < 1$, and $w_0 \approx 1$, when the system is in the insulator-like (top panels), in between the insulator-like and the metallic-like (middle panels), and close to the metallic-like regime (bottom panels), that is for $b = 0.1$, 1, and 10, respectively. In the insets, the phase distribution $\mathcal{P}(\Phi)$ is shown for a coupling strength $|\langle S(w_0) \rangle| \approx 0.5$. The histograms in red lines correspond to numerical results while the continuous black lines correspond to the analytical distribution of Eq. (5). For $b = 0.1$ and 1, the histograms show two peaks around $\Phi = \pi$ which vanish for $b = 10$, i.e., when the system displays a metallic behavior. In the latter, a good agreement with the RMT prediction is observed.

The phase distribution in the perfect coupling regime for the PBRM model at criticality with $\beta = 1$ (first column), 2 (second column), and 4 (third column) symmetries is shown in Fig. 2. The wire lengths are indicated in Fig. 2(g) while the values of parameter b are indicated in each panel. The symbols are obtained by numerical simulations while the solid lines are
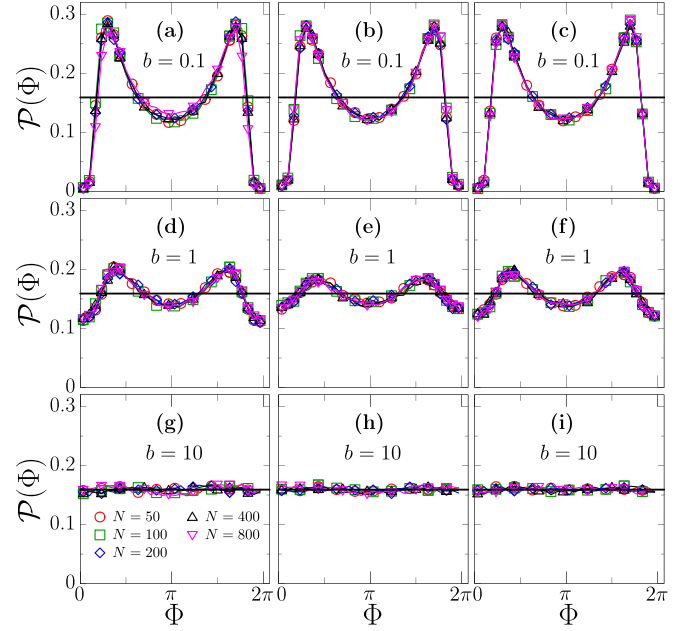

FIG. 2. Phase distribution in the perfect coupling regime, $|\langle S \rangle| \sim 0$, for the PBRM model at criticality for several wire lengths N as indicated in panel (g) and several values of b, as indicated in each panel. The symmetries are $\beta = 1$ (first column), 2 (second column), and 4 (third column). Symbols correspond to numerical results while black lines correspond to the RMT prediction (5).

the RMT prediction of Eq. (5). Again, two big peaks around $\Phi = \pi$ show up when the system is close to the insulator-like regime $b = 0.1$ (top panels) which tend to disappear as b increases (middle and bottom panels). When the system attains a metallic behavior, $b = 10$ (bottom panels), the phase is uniformly distributed around $1/2\pi$, in accordance with the RMT prediction (5). It is also clear that $\mathcal{P}(\Phi)$ does not depend on the wire length nor the symmetry (orthogonal, unitary, or symplectic), as expected in the one open-channel setup [3].

B. Wigner delay time and resonance widths

The delay experienced by a quantum particle due to its interactions with a scattering region is described by the so-called Wigner delay time τ_W. Near the center of the spectrum ($E = 0$), it is given by [42,48]

$$\tau_W(E = 0) = \left. \frac{d\Phi(E)}{dE} \right|_{E=0} = -2 \, \text{Im} \, \text{Tr}(E - H_{\text{eff}})^{-1}|_{E=0}. \tag{6}$$

In the metallic regime and for the one open-channel setup, the distribution of the Wigner delay time is known for all symmetry classes $\beta = 1, 2,$ and 4 [49–52], namely

$$\mathcal{P}(\tau_W) = \frac{2/\beta}{(\beta/2)!} \left(\frac{\beta}{2\tau_W} \right)^{2+\beta/2} e^{-\beta/2\tau_W}. \tag{7}$$

On the other hand, the poles of the scattering matrix show up as resonances which in turn are the complex eigenvalues $\mathcal{E}_n = E_n - i\Gamma_n/2$ of the effective non-Hermitian Hamiltonian H_{eff} [see Eq. (3)], with E_n and Γ_n respectively the position and width of the nth resonance. Furthermore, the resonance width Γ_n is related to the lifetime of the nth resonance as
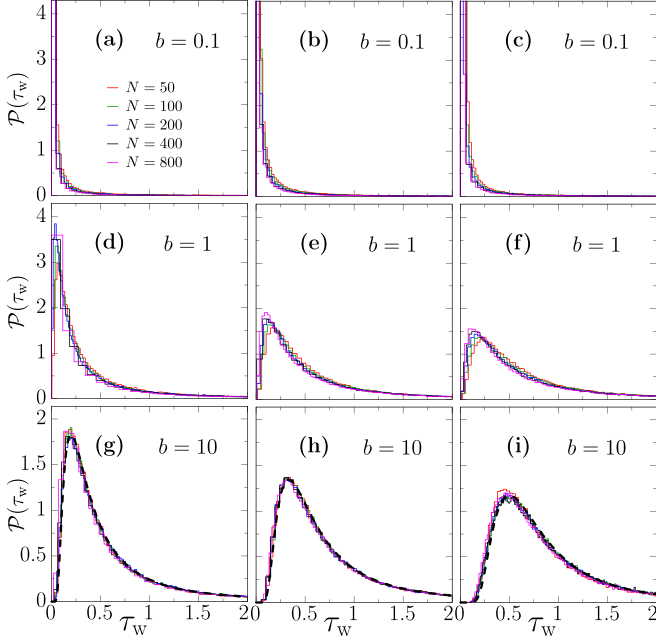
FIG. 3. Distribution of the Wigner delay time for the PBRM model at criticality for several wire lengths N, as indicated in panel (a). The symmetries are $\beta = 1, 2$, and 4, in the first, second, and third columns, respectively. The different values of b are indicated in each panel. The histograms are obtained through Eq. (6), with the normalization constant $w_0^2 \pi / (2L)$, in the perfect coupling regime. The dashed black lines (bottom panels) correspond to the RMT prediction of Eq. (7).

FIG. 4. Distribution of logarithm of resonance widths, normalized to its typical value, for the PBRM model at criticality with $\beta = 1, 2$, and 4, in the first, second, and third columns, respectively. The system sizes N are indicated in panel (g). The values of the bandwidth are indicated in each panel. The insets show the scaling law $\Gamma^{\mathrm{typ}} \propto N^{-\lambda}$. The black dashed lines are the best fitting of the scaling law to the numerical data. The error bars are smaller than the symbols.

$\tau_n = 1/\Gamma_n$, and hence a relationship between Γ_n and the Wigner delay time is expected. These quantities, delay times and resonance widths, have been of pivotal importance in the realm of complex scattering both theoretically and experimentally [39,42,48–59], where recent progress has been made to extend their study to wave-chaotic scattering systems in the presence of absorption [60,61]. For the PBRM model at the critical point, to our knowledge, exact theoretical results for the resonance statistics are scarce; nonetheless, recent progress has been reported for resonance statistics in standard banded matrices in both weak and strong localization regimes [62].

The distribution of the Wigner delay time for the PBRM model at criticality is reported in Fig. 3 for the three symmetry classes $\beta = 1, 2$, and 4, in the first, second, and third columns, respectively. The values of the bandwidth b are shown in each panel. For $b = 0.1$ (top panels), $\mathcal{P}(\tau_W)$ has its maximum at $\tau_W \sim 0$; that is, the system is in the localized regime and conduction is suppressed. For $b = 1$ (middle panels), relatively small time delays dominate, meaning that the system is neither an insulator nor a conductor. For $b = 10$ (bottom panels), the distribution of τ_W is well described by its RMT prediction (7) which sets the system in a metallic-like regime.

The logarithm of the distribution of the resonance widths, normalized to its typical value $\Gamma^{\mathrm{typ}} \equiv \exp\langle \ln \Gamma \rangle$, for the PBRM model at criticality with $\beta = 1$ (first column), 2 (second column), and 4 (third column) are shown in Fig. 4. The wire lengths under consideration are indicated in Fig. 4(g),
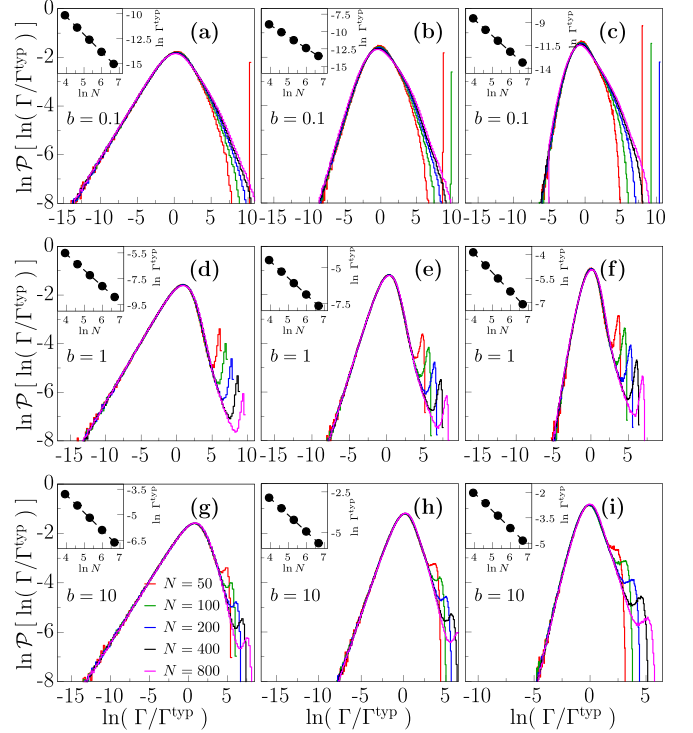
and the different values of b in each panel. For the histograms, only 25% of the eigenvalues around the center of the spectrum, $E = 0$, are used. The typical value Γ^{typ} follows a power law with respect to the wire length N, $\Gamma^{\mathrm{typ}} \propto N^{-\lambda}$, as observed in the insets of the same figure. There, the dashed lines are the best fittings to the numerical data. The resulting exponents λ for each case are reported in Table I.

C. Wigner delay time vs spectral and eigenstate properties of the isolated PBRM model

It is well known that the spatial fluctuations of the eigenstates of disordered systems at criticality show multifractal behavior [4,6,9,63–65]. This behavior is characterized by a set of *generalized dimensions* D_q or *multifractal dimensions*, where q is a real number. Furthermore, the multifractal properties of the eigenstates can also be studied through the Wigner delay time, as shown below.

For disordered systems at criticality, a relationship between the inverse moments of the Wigner delay time and the multifractal dimensions of the eigenstates of the corresponding isolated system D_q is given by [39,47,66],

$$\langle \tau_W^{-q} \rangle \propto N^{-\sigma_q}, \quad \text{where} \quad \sigma_q \equiv q \, D_{q+1} \tag{8}$$

and for the PBRM model at criticality the following functional form for σ_q as a function of the bandwidth b has been proposed

TABLE I. Values of the parameters obtained from the power-law fittings to the data of the insets in Figs. 4–6.

	b	Inset panel	Fig. 4 $\Gamma^{\text{typ}} \propto N^{-\lambda}$ λ	Fig. 5 $\langle \tau_W^{-1} \rangle \propto N^{-\sigma_q}$ σ_q	Fig. 6 $\tau^{\text{typ}} \propto N^{\sigma_\tau}$ σ_τ
$\beta = 1$	0.1	(a)	1.7647 ± 0.0072	0.1404 ± 0.0037	0.2507 ± 0.0048
	1	(d)	1.2265 ± 0.0080	0.7133 ± 0.0068	0.8465 ± 0.0055
	10	(g)	1.0276 ± 0.0213	0.9439 ± 0.0180	0.9586 ± 0.0163
$\beta = 2$	0.1	(b)	1.6424 ± 0.0036	0.2282 ± 0.0034	0.3744 ± 0.0035
	1	(e)	1.1490 ± 0.0063	0.8469 ± 0.0023	0.9217 ± 0.0027
	10	(h)	1.0187 ± 0.0244	0.9609 ± 0.0192	0.9685 ± 0.0204
$\beta = 4$	0.1	(c)	1.7223 ± 0.0245	0.1699 ± 0.0052	0.2990 ± 0.0023
	1	(f)	1.1596 ± 0.0068	0.8499 ± 0.0060	0.9257 ± 0.0040
	10	(i)	1.0218 ± 0.0456	0.9590 ± 0.0175	0.9680 ± 0.0196

[32]

$$\sigma_q \approx \frac{q}{1 + (\alpha_{q+1}b)^{-1}} \tag{9}$$

with α_q being fitting constants. In addition, for PBRM models at criticality, the typical value of the Wigner delay time, defined as $\tau_W^{\text{typ}} \equiv \exp\langle \ln \tau_W \rangle$, obeys the scaling law given by [40]

$$\tau_W^{\text{typ}} \propto N^{\sigma_\tau}, \quad \text{where} \quad \sigma_\tau \equiv D_1. \tag{10}$$

For completeness, the *level compressibility* χ, a quantity often used to characterize the fluctuations of spectra of disordered systems at criticality, is also analyzed. In the metallic [insulator] regime $\chi = 0$ [$\chi = 1$] while at intermediate regimes (neither metallic nor insulator) $0 < \chi < 1$ [67,68]. For PBRM models in the presence of $\beta = 1$ and 2 symmetries, the level compressibility as a function of b is given by [6,36]

$$\chi = \begin{cases} 1 - 4b, & \beta = 1, b \ll 1, \\ 1 - \pi\sqrt{2}b + \frac{4}{3}(2 - \sqrt{3})\pi^2 b^2, & \beta = 2, b \ll 1, \\ 1/2\beta\pi b, & b \gg 1. \end{cases} \tag{11}$$

In addition a heuristic relation between χ and σ_q is also known, namely [32]

$$\chi \approx \frac{q - \sigma_q}{q(\sigma_q + 1)}. \tag{12}$$

In Fig. 5, the distribution of the logarithm of the first inverse moment of the Wigner delay time for the PBRM model at criticality is reported. The values of the bandwidth b and wire lengths N are indicated in the panels. The insets show $\ln\langle \tau_W^{-1} \rangle$ vs $\ln N$ as dots while the dashed lines correspond to fittings to the numerical data with Eq. (8). The resulting exponents σ_q from the fittings are reported in Table I. A good agreement between the numerical data and the scaling law of Eq. (8) is observed.

The behavior of the logarithm of the distribution of $\ln(\tau_W/\tau_W^{\text{typ}})$ for the PBRM model at criticality with the three symmetry classes $\beta = 1$, 2, and 4, for different wire lengths N [see Fig. 5(g)], and different bandwidths b, is plotted in Fig. 6. The insets show the logarithm of τ_W^{typ} as a function of $\ln N$. The dots correspond to numerical results while the dashed lines correspond to fittings with the scaling law of Eq. (10) to the numerical data. The exponents σ_τ resulting from the

fittings are reported in Table I. A good agreement between the numerical data and the scaling law (10) is observed.

In Fig. 7, the multifractal dimension D_q as a function of the bandwidth b for several values of q is plotted. Figures 7(a)–7(c) correspond to the system in the presence of the $\beta = 1$, 2, and 4 symmetry, respectively. The empty symbols are computed by direct diagonalization of the isolated PBRM mode at criticality (see also Ref. [37] for more details). The filled symbols are obtained from the scaling law (8) and the dashed
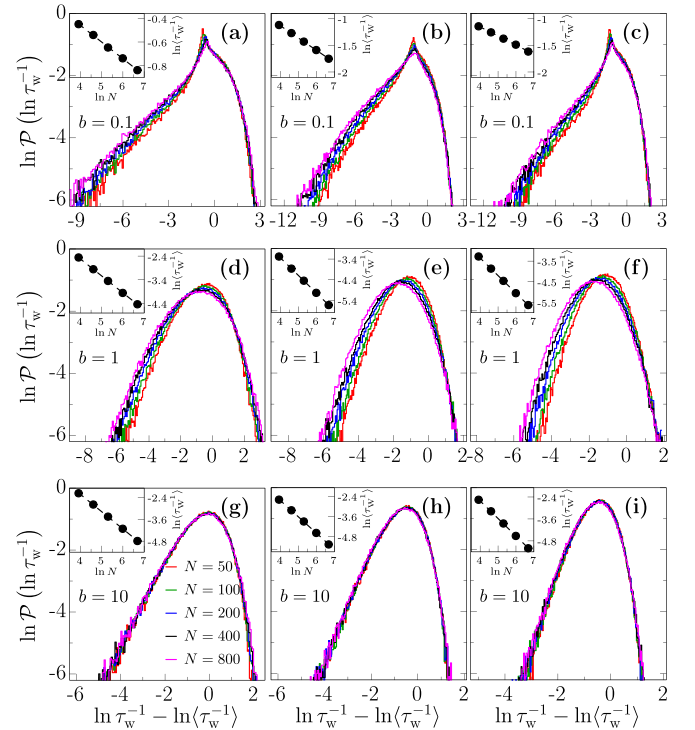

FIG. 5. Distribution of the first inverse moment of the Wigner delay time for the PBRM model at criticality in the presence of the $\beta = 1$ (first column), 2 (second column), and 4 (third column) symmetries. In top panels $b = 0.1$, in middle panels $b = 1$, and in bottom panels $b = 10$. The wire lengths N are indicated in panel (g). The insets show the best fitting (black dashed lines) using the scaling law (8) to the numerical data (symbols). The error bars are smaller than the symbols size.
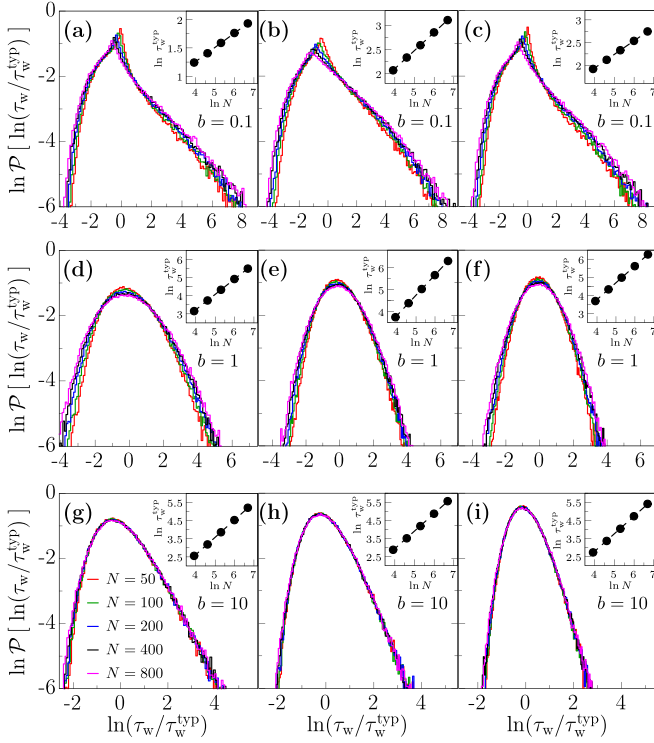
FIG. 6. Distribution of the Wigner delay time normalized to its typical value for the PBRM model at criticality. The symmetry classes are $\beta = 1$ (first column), 2 (second column), and 4 (third column). The bandwidth b is indicated in the panels and the wire lengths N are indicated in panel (g). The insets show fittings of the scaling law (10) (dashed lines) to the numerical data (dots). The error bars are smaller than the symbol size.

lines correspond to Eq. (9) with the α_{q+1} taken from Ref. [37]. These values of α_{q+1} are: 3.33 (5.70, 4.82), 2.55 (4.45, 3.82), 2.11 (3.73, 3.22), 1.52 (2.74, 2.41), and 1.21 (2.22, 1.98) for $\beta = 1$ (2, 4) and $q = 0.2$, 0.6, 1, 2, and 3, respectively [37]. For the three symmetry classes $\beta = 1$ (a), 2 (b), and 4 (c) a good correspondence between the direct calculation of D_q (empty symbols) and the analytics (dashed lines) is found. These results show that for the one channel setup, the multifractal properties of the isolated PBRM model at criticality
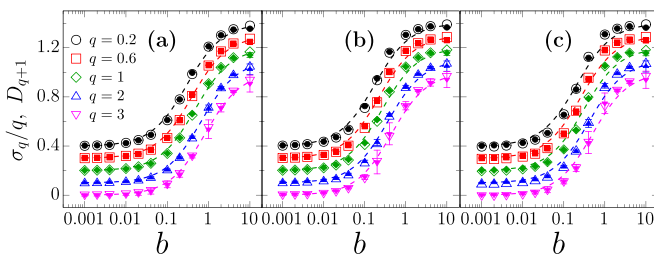

FIG. 7. Multifractal dimensions D_q for the PBRM model at criticality as a function of the bandwidth b. The empty symbols are obtained from direct diagonalization of the closed system (1). The filled symbols correspond to results obtained from the scaling law (8). The dashed lines correspond to the heuristic relation (9). The error bars are the rms of the residuals. For the sake of clarity, the symbols (lines) are displaced vertically upward.
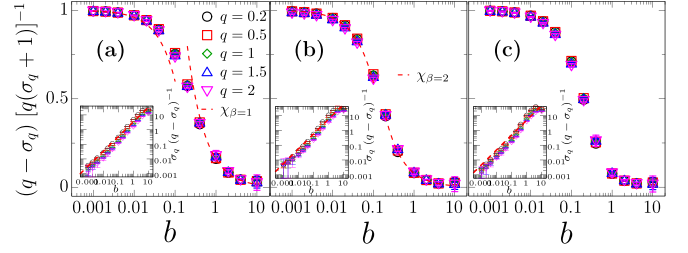

FIG. 8. Level compressibility of the PBRM model at criticality as a function of the bandwidth b. The symmetries are $\beta = 1, 2$, and 4, in panels (a)–(c), respectively. The symbols are obtained from Eq. (12), the dashed red lines correspond to expression (11). Inset: Recursive relation (13), the dashed red lines ($\sim b$) are plotted to guide the eye. The error bars are the rms of the residuals.

can be directly extracted from Wigner delay time, a transport property. This is convenient from an experimental point of view.

In Fig. 8 the spectral compressibility of the PBRM model at criticality is reported. The symbols are obtained from Eq. (12) with the σ_q extracted from the scaling law (8). The dashed lines correspond to the theoretical prediction of Eq. (11). For the PBRM model in the presence of the symmetry classes, $\beta = 1$ and 2, Figs. 8(a) and 8(b), respectively, a good agreement with the analytics is observed. For the $\beta = 4$ case, there is no theoretical prediction available to compare with. However, the following recursive relation [32]:

$$\sigma_q(q - \sigma_q) \approx \alpha_{q+1} b \qquad (13)$$

is known. Then, the PBRM model in the $\beta = 4$ case can also be contrasted with this last relation. For this purpose, in the insets of Fig. 8, the recursive relation (13) (symbols) is shown. The dashed lines are $\sim b$. A good agreement with the numerical data (symbols) is observed.

To this point, the analysis of the PBRM model at criticality with one open channel has been performed. In the next sections, the setup in which the scattering system supports M open channels is studied and contrasted with available RMT predictions.

IV. PBRM MODEL WITH M OPEN CHANNELS

In this section, the analysis of the scattering and transport properties of the PBRM model at criticality with M open channels is presented. As in the previous section, this is performed following the scattering matrix approach of Eq. (3). As shown in Sec. III for the one open-channel setup, the scattering and transport properties of the PBRM model at criticality do not change significantly with the wire length N. A similar behavior has also been found for the M open-channel setup in the $\beta = 1$ case [39–41]. Here this has also been verified for the $\beta = 2$ and 4 cases (not shown). Therefore, in what follows the wire length is set to $N = 50$. For the statistical analysis, 10^6 realizations of the scattering matrix S in the perfect coupling regime are considered. In the same line as in Sec. III, known analytical RMT predictions are presented first and later they are compared with numerical simulations in the appropriate limits.

A. Scattering properties

Within the RMT approach of quantum transport, the average of the magnitude of the elements of the scattering matrix S has been obtained [2]. That is,

$$\langle |S_{nm}|^2 \rangle_{\text{RMT}} = \frac{1 - (1 - 2/\beta)\delta_{n,m}}{M - 1 + 2/\beta}, \quad (14)$$

where β is the symmetry class present in the system, M is the number of open channels, and δ_{nm} is the usual Kronecker delta.

From Eq. (14) and based on numerical simulations for the $M = 2$ open-channel case, it has been conjectured that the average of the S-matrix elements, $\langle |S_{12}|^2 \rangle$ and $\langle |S_{11}|^2 \rangle$, can be expressed as a function of the bandwidth b [41,43]. These are given by

$$\langle |S_{12}|^2 \rangle(b) = \frac{\langle |S_{12}|^2 \rangle_{\text{RMT}}}{1 + (\varepsilon b)^{-2}} \quad \text{and} \quad (15)$$

$$\langle |S_{11}|^2 \rangle(b) = 1 - \langle |S_{12}|^2 \rangle, \quad (16)$$

where ε is a free parameter to be determined by the best fitting to the numerical data. Furthermore, by using a phenomenological expression that relates the bandwith b with the correlation dimension D_2, which is a broadly accepted measure of the spatial extension of the eigenfunctions of disordered systems at the critical point, Eqs. (15) and (16) can also be written in terms of D_2 [41,43]. For the $\beta = 1$ case one gets

$$\langle |S_{12}|^2 \rangle(D_2) = \frac{\langle |S_{12}|^2 \rangle_{\text{RMT}}}{1 + (\kappa/\varepsilon)^2 \left(D_2^{-1} - 1 \right)^2} \quad \text{and} \quad (17)$$

$$\langle |S_{11}|^2 \rangle(D_2) = 1 - \langle |S_{12}|^2 \rangle(D_2), \quad (18)$$

where κ is a fitting parameter and ε is obtained from Eq. (15). Meanwhile, for the $\beta = 2$ and 4 cases one gets

$$\langle |S_{12}|^2 \rangle(D_2) = \begin{cases} \frac{\langle |S_{12}|^2 \rangle_{\text{RMT}}}{1 + (\kappa D_2/\pi)^{-2}}, & b \ll 1, \\ \frac{\langle |S_{12}|^2 \rangle_{\text{RMT}}}{1 + [2\pi(1 - D_2)/\rho]^2}, & b \gg 1, \end{cases} \quad (19)$$

$$\langle |S_{11}|^2 \rangle(D_2) = 1 - \langle |S_{12}|^2 \rangle(D_2), \quad (20)$$

where κ and ρ are fitting parameters, different for each symmetry class β. Notice that the expressions (15), (17), and (19) were obtained heuristically and its analytical derivation remains to be proven, while the relations (16), (18), and (20) are a consequence of the flux conservation condition of the S matrix. However, as shown below, these equations describe well the numerical data.

In Fig. 9 the average of the S-matrix elements, when the PBRM model at criticality supports $M = 2$ open channels, is shown for the $\beta = 1, 2,$ and 4 symmetries, in the first, second, and third columns, respectively. The symbols correspond to numerical simulations and the dashed blue lines are the RMT prediction (14) for which $\langle |S_{12}|^2 \rangle_{\text{RMT}} = 1/3, 1/2,$ and $2/3$ for $\beta = 1, 2,$ and 4, respectively. In the same figure, $\langle |S_{11}|^2 \rangle_{\text{RMT}} = 1 - \langle |S_{12}|^2 \rangle_{\text{RMT}}$ is also shown. The dashed red curves in Figs. 9(a)–9(c) correspond to the generalizations of Eqs. (15) and (16) for the $\beta = 1, 2,$ and 4 symmetry, respectively. Figures 9(d)–9(f) show $\langle |S_{12}|^2 \rangle(D_2)$ with the values of D_2 extracted from Fig. 7. The dashed red lines are Eqs. (17)–(20). The obtained fitting parameters ε, κ, and ρ, for each
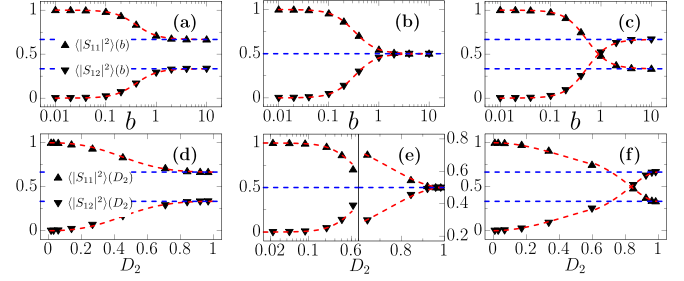

FIG. 9. Average of the S-matrix elements for the PBRM model at criticality with $M = 2$ open channels. The symmetries are $\beta = 1$ (first column), 2 (second column), and 4 (third column). The symbols correspond to numerical simulations, the dashed blue lines are the corresponding RMT prediction (14). Top panels: Average of the S-matrix elements as a function of the bandwidth b. The dashed red lines are Eqs. (15) and (16). Bottom panels: Same as top panels but as a function of the correlation dimension D_2 compared with Eqs. (17)–(20). Error bars are smaller than the symbol size.

symmetry class are reported in Table II. In all the cases, it is observed that for large b and D_2 the model is well described by the RMT predictions while the corresponding generalizations work well for any b and D_2.

B. Transmission and shot noise power

In this section, known analytical results from RMT for the scattering and transport properties of complex media are first revised. Those results are expected to describe the PBRM model at criticality in the case of $b \gg 1$, i.e., in the metallic-like regime.

It is well established that given a scattering problem, the transmission coefficient can be obtained from the elements of the scattering matrix as

$$T = \text{Tr}(t \, t^\dagger), \quad (21)$$

where Tr is the trace operation, t is the transmission amplitude [see Eq. (3)], and the symbol $\dagger$ represents the adjoint of t.

For the $M = 2$ open-channel setup, or two single-channel leads attached to a complex scattering media, the transmission distribution is given by [2]

$$\mathcal{P}(T) = \tfrac{1}{2}\beta T^{-1+\beta/2}, \quad 0 < T < 1, \quad (22)$$

for the symmetry class labeled by β.

Also, for the $M = 4$ open-channel setup, or four single-channel leads attached to a complex scattering media, the

TABLE II. Values of the parameters obtained by fittings to the data of Fig. 9.

β	ε	κ	ρ
1	2.5129 ± 0.0017	2.1043 ± 0.0242	
2	3.0618 ± 0.0022	4.7867 ± 0.0017	2.7857 ± 0.0065
4	1.9359 ± 0.0030	3.9909 ± 0.0078	1.8036 ± 0.0038

distribution of T for the $\beta = 1$ case is [3]

$$\mathcal{P}(T) = \begin{cases} \frac{3}{2}T, & 0 < T < 1, \\ \frac{3}{2}(T - 2\sqrt{T-1}), & 1 < T < 2, \end{cases} \quad (23)$$

while for the $\beta = 2$ case it is [3]

$$\mathcal{P}(T) = \begin{cases} 2T^3, & 0 < T < 1, \\ 2(2 - T)^3, & 1 < T < 2. \end{cases} \quad (24)$$

Now, for the $\beta = 4$ symmetry, following Ref. [3] it is straightforward to arrive at

$$\mathcal{P}(T) = \begin{cases} \frac{12}{7}T^7, & 0 < T < 1, \\ \frac{12}{7}(2 - T)^5(T^2 + 10T - 10), & 1 < T < 2. \end{cases} \quad (25)$$

In general, the tail of the transmission distribution for all β and any number of open channels M decays as [3]

$$\mathcal{P}(T) \propto T^{-1+\beta M^2/2}. \quad (26)$$

Furthermore, for a complex scattering media attached to two leads supporting respectively N_1 and N_2 open channels, the average transmission and its variance are given by [2,69]

$$\langle T \rangle = \frac{N_1 N_2}{N_1 + N_2 - 1 + 2/\beta} \quad (27)$$

and

$$\text{var}(T) = \frac{2N_1 N_2 \left(N_1 - 1 + \frac{2}{\beta}\right)\left(N_2 - 1 + \frac{2}{\beta}\right)}{\beta\left(N_1 + N_2 - 2 + \frac{2}{\beta}\right)\left(N_1 + N_2 - 1 + \frac{4}{\beta}\right)\left(N_1 + N_2 - 1 + \frac{2}{\beta}\right)^2}, \quad (28)$$

for all symmetry classes labeled by β.

Another transport quantity of interest is the so-called shot noise power P, defined as $P = \langle \text{tr}(tt^\dagger - tt^\dagger\, tt^\dagger) \rangle$, whose probability distribution is given by [70]

$$P = \frac{N_1\left(N_1 - 1 + \frac{2}{\beta}\right)N_2\left(N_2 - 1 + \frac{2}{\beta}\right)}{\left(K - 2 + \frac{2}{\beta}\right)\left(K - 1 + \frac{2}{\beta}\right)\left(K - 1 + \frac{4}{\beta}\right)}, \quad (29)$$

where $K = N_1 + N_2$ is the total number of open channels. Note that although the distribution (29) was derived for the $\beta = 1$ and 2 symmetries, it also encompasses the symplectic case, $\beta = 4$, as will be verified below for the PBRM model with $b \to \infty$.

In Eqs. (27)–(29) the number of open channels, N_1 and N_2, may be different. However, in order to compare these quantities with numerical simulations of the PBRM model, we set $N_1 = N_2$ with $M = N_1 + N_2$ the total number of open channels.

For the PBRM model at criticality with two single-channel leads attached to it ($M = 2$ open channels), the transmission distribution for several values of b and $\beta = 1$, 2, and 4 (first, second, and third columns, respectively), is shown in Fig. 10. The red lines correspond to histograms obtained from numerical simulations while the dashed blue lines are Eq. (22) for the respective β. For the three symmetry classes under consideration, a smooth transition from a localized-like to a metallic-like regime is observed as the bandwidth b increases. The metallic-like regime is reached when $b = 4$ for which a good agreement with the RMT prediction (22) is obtained [see Figs. 10(j)–10(l)].

It is instructive to look at the behavior of the transmission distribution $\mathcal{P}(T)$ in the insulator-like regime $b \ll 1$ where RMT predictions are not available. In this regime where $\mathcal{P}(T) \approx 0$ it is more convenient to analyze the distribution of $\ln T$. For the PBRM model at criticality with $M = 2$, the distribution of the logarithm of T for $\beta = 1$ (first column), 2 (second column), and 4 (third column) and several values

of the $b < 1$, as indicated in Fig. 10(g), is shown in Fig. 11. In Figs. 11(a)–11(c), it is observed that the shape and width of $\ln \mathcal{P}(\ln T)$ do not change despite the fact that b varies. This means that $\ln \mathcal{P}(\ln T)$ should be scale invariant, a property that was confirmed before for $\beta = 1$ with the typical transmission $T^{\text{typ}} = \exp\langle \ln T \rangle$ as scaling parameter. Also note in Figs. 11(d)–11(f) that $\langle \ln T \rangle \sim \ln b$ for $b < 1$. Indeed, all distributions $\ln \mathcal{P}(\ln T)$ fall on top of each other when plotted as a function of $\ln(T/T^{\text{typ}})$, as shown in Figs. 11(g)–11(i). We stress that this behavior has previously been reported for the PBRM model in the presence of the $\beta = 1$ symmetry but neither for the $\beta = 2$ (periodic) nor for the $\beta = 4$ symmetries.

Since the tails of the distribution $\mathcal{P}(T)$ from the PBRM model in the metallic-like regime ($b \to \infty$) are expected to correspond to Eq. (26), then it is reasonable to assume that those tails may be described by

$$\mathcal{P}(T) \propto T^\nu \quad (30)$$

for all b, with ν a fitting parameter. Furthermore, for the PBRM model with $\beta = 1$ symmetry, in Ref. [38] the following relationship between the exponent ν and the correlation dimension D_2:

$$\nu(D_2) \propto (1 - D_2)^2, \quad b \gg 1, \quad (31)$$

has been proposed.

The asymptotic behavior of the transmission distribution for the PBRM model at criticality as a function of the bandwidth b and of the correlation dimension D_2 is analyzed in Fig. 12 for the $\beta = 1$, 2, and 4 symmetries in the first, second, and third columns, respectively. In Figs. 12(a)–12(c), for each value of b the corresponding exponent ν (red inverted triangles) is obtained from the best fitting of Eq. (30) to the numerical data for $T > 0.5$. The exponent ν as a function of D_2 is shown in Figs. 12(d)–12(f). The relationship between D_2 and the bandwidth $b \gg 1$ is given by $D_2(b) = 1 - (2\pi b)^{-1}$ [6,38]. In all panels the dashed blue lines are the RMT
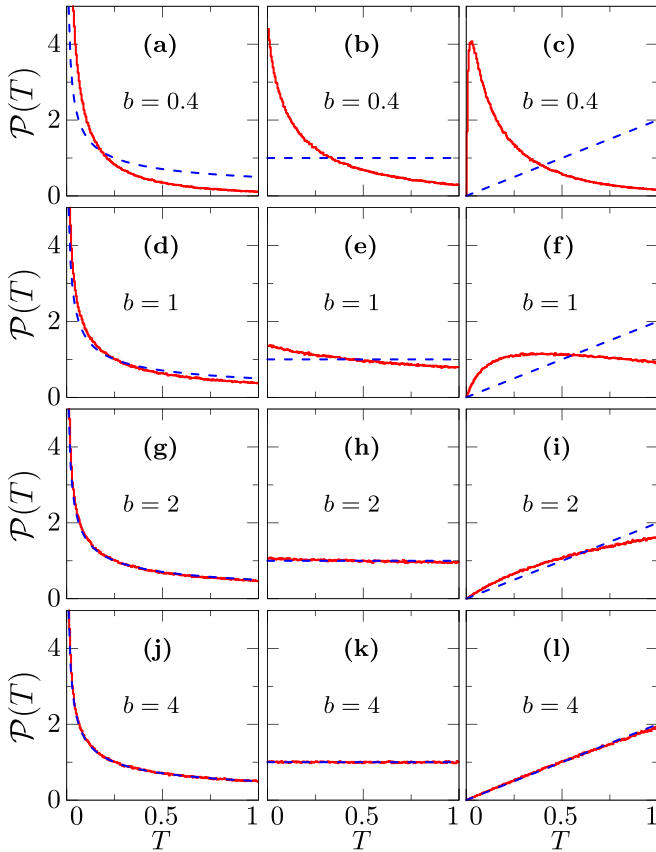
FIG. 10. Transmission distribution of the PBRM model at criticality with $M = 2$ open channels and several values of b. The symmetries are $\beta = 1, 2$, and 3, in the first, second, and third columns, respectively. The red lines correspond to histograms obtained from numerical simulations while the dashed blue lines are the RMT prediction (22) for the respective β. A smooth transition from localized-like to metallic-like regime is observed for the three symmetry classes.

prediction (26) according to the symmetry class. The dashed black lines are the best fittings to the numerical data, which are proportional to b^{-2} (top panels) and to $(1 - D_2)^2$ (bottom panels). The latter shows that the relationship (31) is valid for $D_2 > 0.75$.

The transmission distribution for the PBRM model at criticality with four single-channel leads attached it ($M = 4$) is reviewed in Fig. 13. The symmetries are $\beta = 1, 2$, and 4, in the left, middle, and right panels, respectively, and the considered values of b are indicated in the panels. The red lines are histograms obtained from numerical simulations, and the dashed blue lines are the RMT predictions (23)–(25) according to the symmetry class. For each case, a smooth transition from an insulator-like to a metallic-like regime is observed. In Figs. 13(j) and 13(k), the metallic-like regimen is reached for values of $b = 4$ when the system is in the presence of the orthogonal and the unitary symmetry, respectively. However, when the system is in the presence of the symplectic symmetry, a larger value of b ($= 10$) is required to reach the metallic-like phase, as shown in Fig. 13(l). Close to the insulator-like regime ($b < 0.5$), the transmission distribution shows a pretty similar behavior to that obtained for
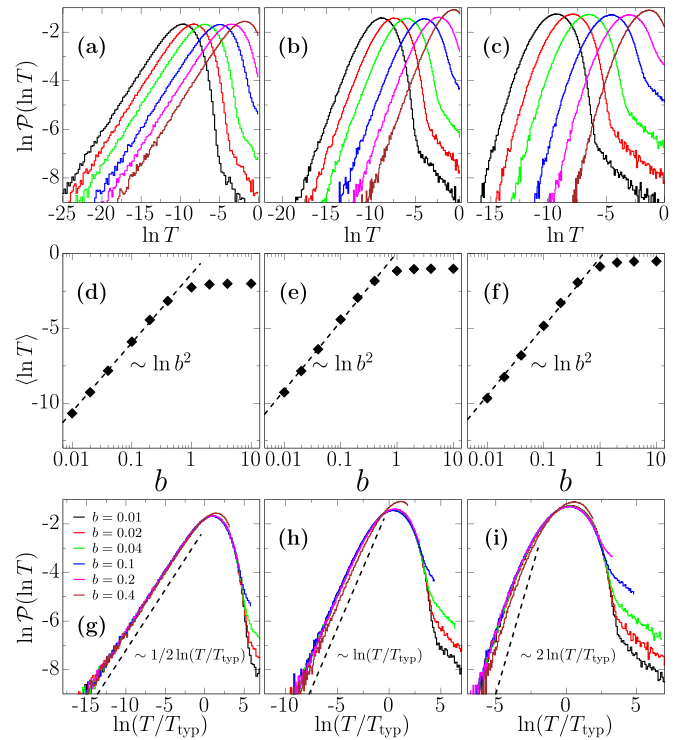

FIG. 11. Distribution of the logarithm of transmission for the PBRM model at criticality with $M = 2$ and several values of the bandwidth b, as indicated in panel (g). The symmetries are $\beta = 1$ (first column), 2 (second column), and 4 (third column). The error bars in panels (d)–(f) are smaller than the symbol size. See text for the discussion.
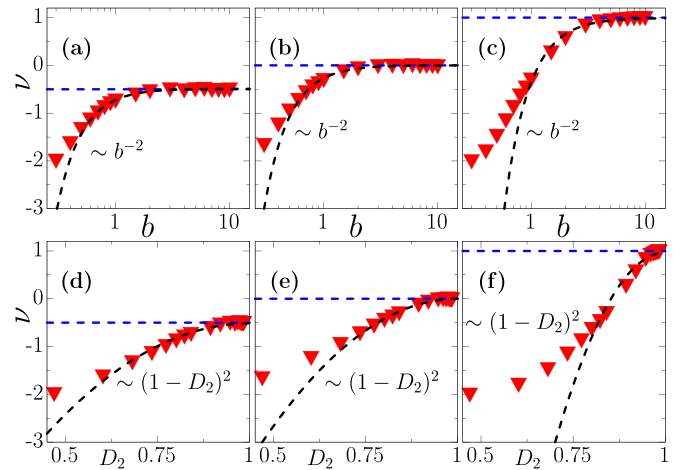

FIG. 12. Exponents ν extracted from the best fitting of Eq. (30) to the numerical transmission distribution of the PBRM model at criticality for $M = 2$. The symmetries are $\beta = 1, 2$, and 4, in the first, second, and third columns, respectively. Top panels: ν as a function of the bandwidth b. The red inverted triangles correspond to numerical results for $T > 0.5$, the dashed blue lines are the RMT prediction (26) for the corresponding symmetry classes and the dashed black lines are the best fitting of b^2 to the data. Bottom panels: Same as top panels but as a function of the correlation dimension D_2 whose relationship with $b \gg 1$ is given through $D_2(b) = 1 - (2\pi b)^{-1}$ [6,38]. The fittings are performed by using $(1 - D_2)^2$. The error bars are the rms of the residual and are smaller than the symbol size.
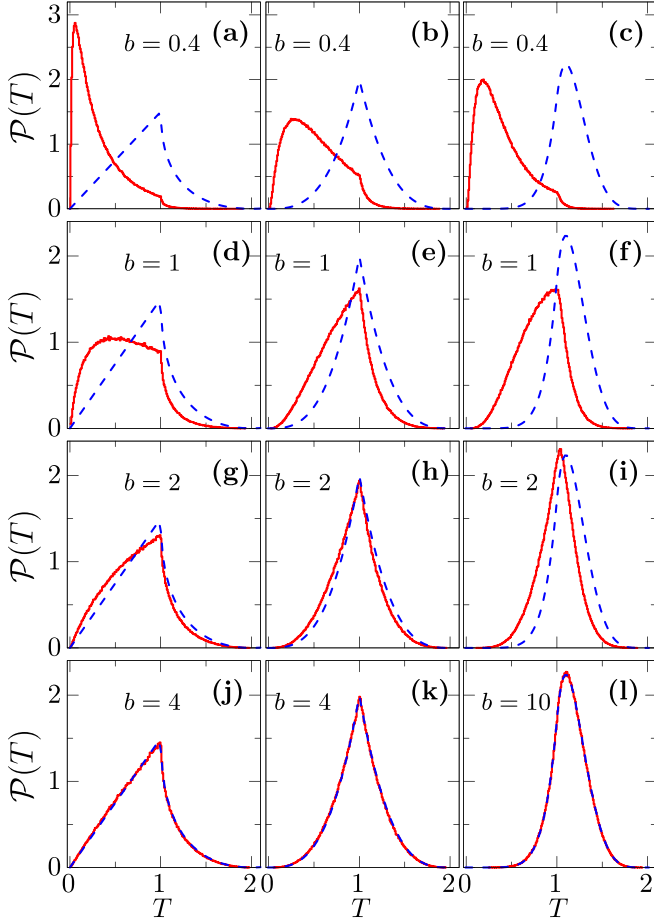
FIG. 13. Transmission distribution of the PBRM model at criticality for $M = 4$ and several values of the effective bandwidth b, as indicated in the panels. The symmetries are $\beta = 1$, 2, and 4 in the left, middle, and right columns, respectively. The red lines are histograms obtained by numerical simulations and the dashed blue lines are the corresponding RMT predictions (23)–(25).
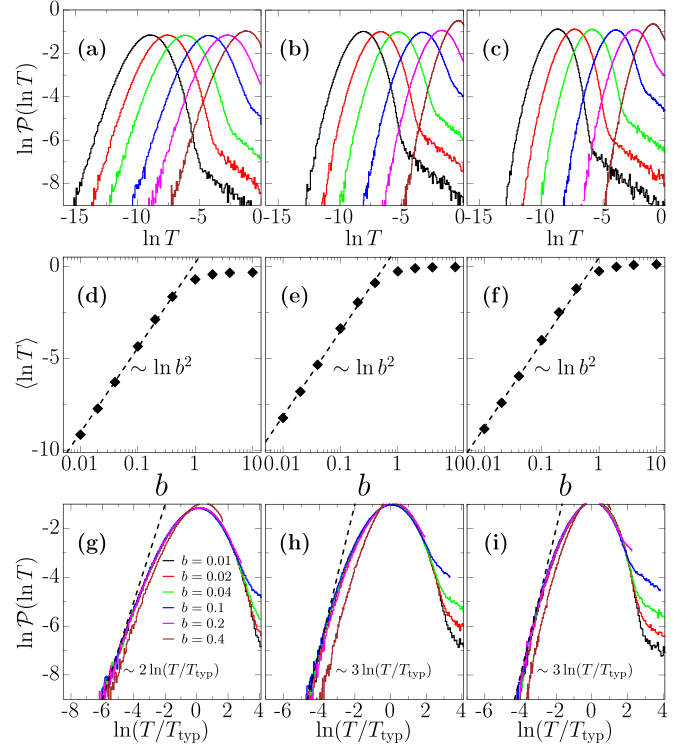

FIG. 14. Distribution of the logarithm of transmission of the PBRM model at criticality with $M = 4$ and several values of the bandwidth b, as indicated in panel (g). The symmetries are $\beta = 1$ (first column), 2 (middle column), and 4 (third column). The error bars in panels (d)–(f) are smaller than the symbol size.

the $M = 2$ case, as observed in Fig. 14 (see also Fig. 11). There, $\ln \mathcal{P}(\ln T)$ also shows a scaling property, i.e., all the curves fall on top of each other when normalized to its typical value $T^{\text{typ}} = \exp\langle \ln T \rangle \sim b^2$, as observed in Figs. 13(g)–13(i). Also, $\langle \ln T \rangle$ is a linear function of $\ln b$ for $b < 1$, see Figs. 13(d)–13(f).

For the PBRM model at criticality with $\beta = 1$ symmetry, it has been conjectured that the averages $\langle T \rangle$, $\text{Var}(\langle T \rangle)$, and P, as a function of the bandwidth b, obey the following expression:

$$X(b) = X_{\text{RMT}}\left[\frac{1}{1 + (\delta \, b)^{-2}}\right], \tag{32}$$

where X may be $\langle T \rangle$, $\text{Var}(\langle T \rangle)$, or P; X_{RMT} is the corresponding RMT prediction and δ is a fitting parameter. In what follows, this conjecture is verified for the PBRM model at criticality for the $\beta = 2$ and 4 symmetries. For the $\beta = 1$ case is also reviewed. For the numerical analysis, the wire length is set to $N = 200$ and 10^5 realizations of the S matrix of Eq. (3) are generated.

In Figs. 15(a)–15(c), for the PBRM model at criticality $\langle T \rangle$ as a function of the open channels M is shown for $\beta = 1$, 2, and 4, in the first, second, and third columns, respectively, and for several values of b. The symbols correspond to numerical results while the dashed blue lines are the RMT predictions (27) according to the symmetry class. The red horizontal line at $\langle T \rangle = 0$ is shown to guide the eye. In those panels, it is observed that for the three symmetry clases at small $b < 0.2$, $\langle T \rangle \approx 0$ since the system is in the insulator-like regime. As b increases ($0.2 \leqslant b < 4$) the average transmission also increases until it reaches the RMT prediction ($b = 10$) where the system is in the metallic-like regime. For the three symmetry classes labeled by β, Eq. (27) gives an accurate description even though deviations appear for the $\beta = 4$ case when $M \geqslant 4$. In the bottom panels the conjecture (32) for $\langle T \rangle$, normalized to its RMT prediction (27), as a function of δb for $\beta = 1$ [Fig. 15(d)], 2 [Fig. 15(e)], and 4 [Fig. 15(f)], is shown. The symbols are obtained from numerical simulations while the dashed blue and dashed red lines, at $\langle T \rangle = 1$ and 0 respectively, are shown to guide the eye. In this case, the conjecture correctly describes the numerical data as can be seen by the shape described by the symbols and more clearly in the small error bars shown in the insets, which are not even visible since they are smaller than the symbols.

In Fig. 16, the results for the variance of T as a function of M for the PBRM model at criticality are reported for several values of b and for the symmetries $\beta = 1$, 2, and 4, in the first, second, and third columns, respectively. In the top panels,
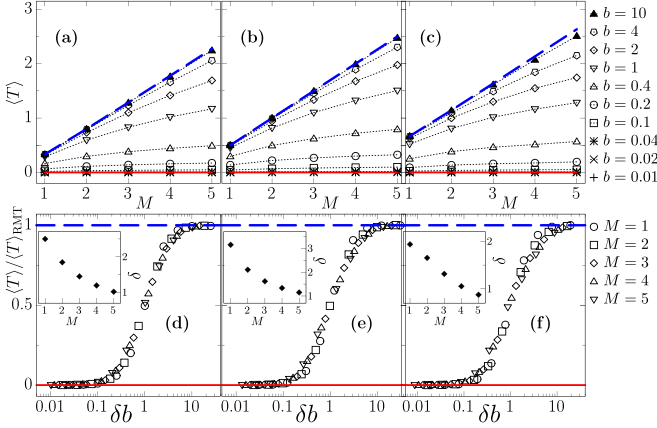
FIG. 15. Average transmission for the PBRM model at criticality with symmetry $\beta = 1$, 2, and 4, in the first, second, and third columns, respectively. Top panels: $\langle T \rangle$ as a function of M for several values of the bandwidth b. The symbols correspond to numerical simulations, the dashed blue lines are the RMT predictions (27), and the red line at $\langle T \rangle = 0$ is plotted to guide the eye. Bottom panels: Conjecture (32) for $\langle T \rangle$, the symbols correspond to numerical simulations. Insets: Fitting parameter from (32) for each M, the error bars are the rms of the residuals and are smaller than the symbol size.

FIG. 17. Shot noise power P for the PBRM model at criticality with symmetry $\beta = 1$ (first column), 2 (second column), and 4 (third column). Top panels: P as a function of M for several values of the bandwidth b, the symbols correspond to numerical results, the dashed blue lines are the RMT predictions (29), and the red line at $P = 0$ is shown to guide the eye. Bottom panels: Conjecture (32) for P, the symbols are obtained by numerical simulation. Insets: Fitting parameter from (32) for each M, the error bars are the rms of the residuals.

the symbols are the numerical data, the dashed blue lines are the corresponding RMT prediction (28), and the red line at $\mathrm{var}(T) = 0$ is shown to guide the eye. It can be observed that for $M \geqslant 2$ and certain interval of b, the fluctuations are greater than the RMT predictions. That behavior is more notorious for the $\beta = 2$ and 4 cases in the interval $0.4 \leqslant b \leqslant 4$. However,

in the metallic regime ($b = 10$), a good agreement with the RMT predictions is obtained.

The $\mathrm{var}(T)$ normalized to its corresponding RMT prediction as a function of δb is plotted in Figs. 16(d)–16(f), for $\beta = 1, 2$, and 4, respectively. For $2 < \delta b < 40$ and $M \geqslant 2$ large deviations between the conjecture (32) (dashed blue line) and the numerical data (symbols) are observed, even though these deviations are smaller for the $\beta = 1$ case. This can also be appreciated in the insets where the error bars are relatively large.

Finally, the shot noise power P as a function of M and for several values of b is reported in the top panels of Fig. 17. A transition from an insulator-like ($b = 0.01$) where $P = 0$ (red horizontal line) to a metallic-like ($b = 10$) regime (symbols) is clearly observed. In the metallic-like regime, the numerical results (symbols) are in agreement with the RMT predictions (29) (dashed blue lines). In the bottom panels of the same figure, the conjecture (32) for P as a function of δb and several values of M is shown. A good agreement between the numerical data and expression (32) is obtained for the three symmetry classes β, as revealed by the shape described by the symbols and the small error bars obtained (see insets).
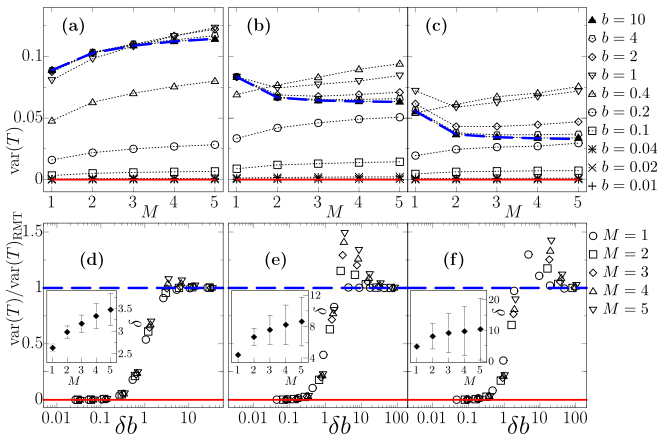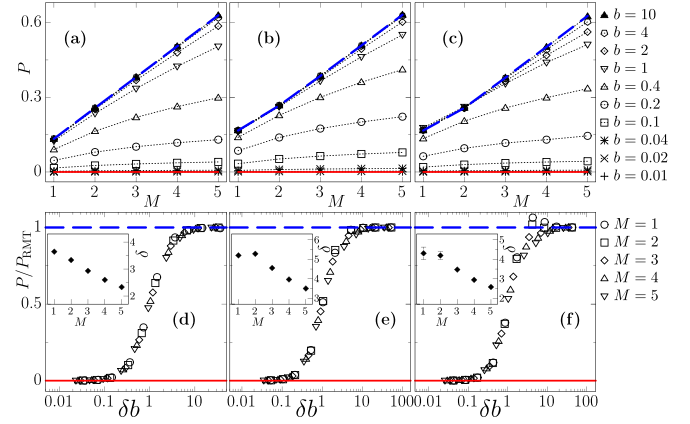

FIG. 16. Variance of transmission for the PBRM model at criticality in the presence of the symmetry $\beta = 1$ (first column), 2 (second column), and 4 (third column). Top panels: $\mathrm{var}(T)$ as a function of M for several values of the bandwidth b, the symbols are the numerical results, dashed blue lines are the RMT predictions (28), and the red line at $\mathrm{var}(T) = 0$ is shown to guide the eye. Bottom panels: Conjecture (32) for $\mathrm{var}(T)$, normalized to its corresponding RMT prediction. The symbols correspond to numerical simulations while the dashed blue line is the expression (32). Insets: Fitting parameter from (32) for each M. The error bars are the rms of the residuals.

V. CONCLUSIONS

In this paper, an extensive numerical study of the scattering and transport properties of the PBRM model at criticality in the presence of the three symmetry classes, orthogonal, unitary, and symplectic, has been presented. For the sake of completeness, some known results for the orthogonal case previously studied in the literature have also been reviewed, while new ones for the unitary (in the periodic model) and the symplectic cases, which had remained unexplored in the context of the PBRM models, are reported. Surprisingly, the

results presented confirm that the scattering and transport properties of the symplectic PBRM model can be well described by existing analytical and heuristic relations widely used in studies of the PBRM model in the presence of the $\beta = 1$ and 2 symmetries. Importantly, for the three symmetry classes the multifractal properties of the isolated model were obtained from scattering and transport properties, which is very convenient from the experimental point of view since direct access to the eigenfunctions is not required.

Additionally, an analytical result for the transmission distribution in the presence of the symplectic symmetry with $M = 4$ open channels (25), which applies to the symplectic PBRM model at criticality in the metallic regime, was provided. Also, in this study, the results for $\beta = 1$ are in accordance with those reported in, for example, Ref. [41]. Moreover, to our knowledge, our results for $\beta = 2$ have not been reported before; only the nonperiodic version of the PBRM model with broken time-reversal symmetry ($\beta = 2$) has been studied in Ref. [43]. And the symplectic case, $\beta = 4$, has not been reported in neither the periodic nor in the non-

periodic version of the PBRM model so far. Thus, with the present study a more clear panorama about the scattering and transport properties of the PBRM model at criticality in the presence of the three classical Wigner-Dyson symmetries is given.

[1] P. A. Lee and T. V. Ramakrishnan, Disordered electronic systems, Rev. Mod. Phys. **57**, 287 (1985).

[2] C. W. J. Beenakker, Random-matrix theory of quantum transport, Rev. Mod. Phys. **69**, 731 (1997).

[3] P. A. Mello and N. Kumar, *Quantum Transport in Mesoscopic Systems: Complexity and Statistical Fluctuations* (Oxford Universtity Press, New York, 2005).

[4] M. Janssen, Multifractal analysis of broadly-distributed observables at criticality, Int. J. Mod. Phys. B **08**, 943 (1994).

[5] M. Imada, A. Fujimori, and Y. Tokura, Metal-insulator transitions, Rev. Mod. Phys. **70**, 1039 (1998).

[6] F. Evers and A. D. Mirlin, Anderson transitions, Rev. Mod. Phys. **80**, 1355 (2008).

[7] A. Rodriguez, L. J. Vasquez, K. Slevin, and R. A. Römer, Critical Parameters from a Generalized Multifractal Analysis at the Anderson Transition, Phys. Rev. Lett. **105**, 046403 (2010).

[8] P. P. Edwards and C. N. R. Rao, *The Metal-Nonmetal Transition Revisited*, 2nd ed. (CRC Press, London, 2017).

[9] M. Janssen, Statistics and scaling in disordered mesoscopic electron systems, Phys. Rep. **295**, 1 (1998).

[10] B. Huckestein, Scaling theory of the integer quantum hall effect, Rev. Mod. Phys. **67**, 357 (1995).

[11] A. D. Mirlin, Statistics of energy levels and eigenfunctions in disordered systems, Phys. Rep. **326**, 259 (2000).

[12] Y. V. Fyodorov and A. D. Mirlin, Statistical properties of eigenfunctions of random quasi 1d one-particle hamiltonians, Int. J. Mod. Phys. B **08**, 3795 (1994).

[13] Y. V. Fyodorov and A. D. Mirlin, Mesoscopic fluctuations of eigenfunctions and level-velocity distribution in disordered metals, Phys. Rev. B **51**, 13403 (1995).

[14] V. I. Fal'ko and K. B. Efetov, Statistics of prelocalized states in disordered conductors, Phys. Rev. B **52**, 17413 (1995).

[15] F. Wegner, Inverse participation ratio in $2 + \epsilon$ dimensions, Z. Phys. B **36**, 209 (1980).

[16] M. Schreiber and H. Grussbach, Multifractal Wave Functions at the Anderson Transition, Phys. Rev. Lett. **67**, 607 (1991).

[17] A. Mildenberger, F. Evers, and A. D. Mirlin, Dimensionality dependence of the wave-function statistics at the Anderson transition, Phys. Rev. B **66**, 033109 (2002).

[18] A. Bäcker, M. Haque, and I. M. Khaymovich, Multifractal dimensions for random matrices, chaotic quantum maps, and many-body systems, Phys. Rev. E **100**, 032117 (2019).

[19] E. G. Carnio, N. D. M. Hine, and R. A. Römer, Multifractality of ab initio wave functions in doped semiconductors, Phys. E **111**, 141 (2019).

[20] T. Guhr, A. Müller-Groeling, and H. A. Weidenmüller, Random-matrix theories in quantum physics: Common concepts, Phys. Rep. **299**, 189 (1998).

[21] M. L. Mehta, *Random Matrices and the Statistical Theory of Energy Levels* (Academic Press, New York, 2004).

[22] F. J. Dyson, Statistical theory of the energy levels of complex systems. I, J. Math. Phys. **3**, 140 (1962).

[23] F. J. Dyson, Statistical theory of the energy levels of complex systems. II, J. Math. Phys. **3**, 157 (1962).

[24] A. D. Mirlin, Y. V. Fyodorov, F. M. Dittes, J. Quezada, and T. H. Seligman, Transition from localized to extended eigenstates in the ensemble of power-law random banded matrices, Phys. Rev. E **54**, 3221 (1996).

[25] V. E. Kravtsov, Critical spectral statistics as the luttinger liquid of energy levels at a finite temperature, Ann. Phys. **8**, 621 (1999).

[26] I. Varga and D. Braun, Critical statistics in a power-law random-banded matrix ensemble, Phys. Rev. B **61**, R11859 (2000).

[27] J. A. Méndez-Bermúdez, A. Alcazar-López, and I. Varga, Multifractal dimensions for critical random matrix ensembles, Europhys. Lett. **98**, 37006 (2012).

[28] E. Cuevas, M. Ortuño, V. Gasparian, and A. Pérez-Garrido, Fluctuations of the Correlation Dimension at Metal-Insulator Transitions, Phys. Rev. Lett. **88**, 016401 (2001).

[29] V. E. Kravtsov and K. A. Muttalib, New Class of Random Matrix Ensembles with Multifractal Eigenvectors, Phys. Rev. Lett. **79**, 1913 (1997).

[30] V. E. Kravtsov and A. M. Tsvelik, Energy level dynamics in systems with weakly multifractal eigenstates: Equivalence to one-dimensional correlated fermions at low temperatures, Phys. Rev. B **62**, 9888 (2000).

[31] I. Varga, Fluctuation of correlation dimension and inverse participation number at the Anderson transition, Phys. Rev. B **66**, 094201 (2002).

[32] J. A. Méndez-Bermúdez, A. Alcazar-López, and I. Varga, On the generalized dimensions of multifractal eigenstates, J. Stat. Mech. (2014) P11012.

[33] A. D. Mirlin and F. Evers, Multifractality and critical fluctuations at the Anderson transition, Phys. Rev. B **62**, 7920 (2000).

[34] F. Evers and A. D. Mirlin, Fluctuations of the Inverse Participation Ratio at the Anderson Transition, Phys. Rev. Lett. **84**, 3690 (2000).

[35] W.-J. Rao, Power-law random banded matrix ensemble as the effective model for many-body localization transition, Eur. Phys. J. Plus **137**, 398 (2022).

[36] V. E. Kravtsov, O. M. Yevtushenko, and E. Cuevas, Level compressibility in a critical random matrix ensemble: The second virial coefficient (corrigendum), J. Phys. A: Math. Theor. **44**, 189501 (2011).

[37] M. Carrera-Núñez, A. M. Martínez-Argüello, and J. A. Méndez-Bermúdez, Multifractal dimensions and statistical properties of critical ensembles characterized by the three classical Wigner–Dyson symmetry classes, Physica A **573**, 125965 (2021).

[38] J. A. Méndez-Bermúdez, V. A. Gopar, and I. Varga, Conductance distribution at criticality: One-dimensional Anderson model with random long-range hopping, Ann. Phys. (Berlin) **521**, 887 (2009).

[39] J. A. Méndez-Bermúdez and T. Kottos, Probing the eigenfunction fractality using Wigner delay times, Phys. Rev. B **72**, 064108 (2005).

[40] J. A. Méndez-Bermúdez and I. Varga, Scattering at the Anderson transition: Power-law banded random matrix model, Phys. Rev. B **74**, 125114 (2006).

[41] J. A. Méndez-Bermúdez, V. A. Gopar, and I. Varga, Scattering and transport statistics at the metal-insulator transition: A numerical study of the power-law banded random-matrix model, Phys. Rev. B **82**, 125106 (2010).

[42] T. Kottos and M. Weiss, Statistics of Resonances and Delay Times: A Criterion for Metal-Insulator Transitions, Phys. Rev. Lett. **89**, 056401 (2002).

[43] A. Alcazar-López, J. A. Méndez-Bermúdez, and I. Varga, Broken time-reversal symmetry scattering at the Anderson transition, Ann. Phys. (Berlin) **521**, 896 (2009).

[44] C. Mahaux and H. A Weidenmüller, *Shell Model Approach in Nuclear Reactions* (North-Holland, Amsterdam, 1969).

[45] J. J. M. Verbaarschot, H. A. Weidenmüller, and M. R. Zirnbauer, Grassmann integration in stochastic quantum physics: The case of compound-nucleus scattering, Phys. Rep. **129**, 367 (1985).

[46] I. Rotter, A continuum shell model for the open quantum mechanical nuclear system, Rep. Prog. Phys. **54**, 635 (1991).

[47] A. Ossipov and Y. V. Fyodorov, Statistics of delay times in mesoscopic systems as a manifestation of the eigenfunctions fluctuations, Phys. Rev. B **71**, 125133 (2005).

[48] F. Steinbach, A. Ossipov, T. Kottos, and T. Geisel, Statistics of Resonances and of Delay Times in Quasiperiodic Schrödinger Equations, Phys. Rev. Lett. **85**, 4426 (2000).

[49] V. A. Gopar, P. A. Mello, and M. Büttiker, Mesoscopic Capacitors: A Statistical Analysis, Phys. Rev. Lett. **77**, 3005 (1996).

[50] Y. V. Fyodorov and H.-J. Sommers, Statistics of resonance poles, phase shifts and time delays in quantum chaotic scattering: Random matrix approach for systems with broken time-reversal invariance, J. Math. Phys. **38**, 1918 (1997).

[51] Y. V. Fyodorov, D. V. Savin, and H.-J. Sommers, Parametric correlations of phase shifts and statistics of time delays in quantum chaotic scattering: Crossover between unitary and orthogonal symmetries, Phys. Rev. E **55**, R4857(R) (1997).

[52] A. M. Martínez-Argüello, A. A. Fernández-Marín, and M. Martínez-Mares, Delay times in chaotic quantum systems, Eur. Phys. J. Spec. Top. **226**, 519 (2017).

[53] I. Kukulin, M. Krasnopolsky, and J. Horacek, *Theory of Resonances: Principles and Applications* (Kluwer, Dordrecht, 1989).

[54] E. Doron, U. Smilansky, and A. Frenkel, Experimental Demonstration of Chaotic Scattering of Microwaves, Phys. Rev. Lett. **65**, 3072 (1990).

[55] T. Kottos, Statistics of resonances and delay times in random media: Beyond random matrix theory, J. Phys. A: Math. Gen. **38**, 10761 (2005).

[56] Y. V. Fyodorov and D. V. Savin, Statistics of Resonance Width Shifts as a Signature of Eigenfunction Nonorthogonality, Phys. Rev. Lett. **108**, 184101 (2012).

[57] U. Kuhl, R. Höhmann, J. Main, and H.-J. Stöckmann, Resonance Widths in Open Microwave Cavities Studied by Harmonic Inversion, Phys. Rev. Lett. **100**, 254101 (2008).

[58] Y. V. Fyodorov and D. V. Savin, Resonance width distribution in RMT: Weak-coupling regime beyond Porter-Thomas, Europhys. Lett. **110**, 40006 (2015).

[59] M. Novaes, Time delay statistics for finite number of channels in all symmetry classes, Europhys. Lett. **139**, 21001 (2022).

[60] L. Chen, S. M. Anlage, and Y. V. Fyodorov, Generalization of Wigner time delay to subunitary scattering systems, Phys. Rev. E **103**, L050203 (2021).

[61] L. Chen, S. M. Anlage, and Y. V. Fyodorov, Statistics of Complex Wigner Time Delays as a Counter of S-Matrix Poles: Theory and Experiment, Phys. Rev. Lett. **127**, 204101 (2021).

[62] Y. V. Fyodorov, M. A. Skvortsov, and K. S. Tikhonov, Resonances in a single-leadreflection from a disordered medium: σ-model approach, arXiv:2211.03376 (2022).

[63] K. Hashimoto, C. Sohrmann, J. Wiebe, T. Inaoka, F. Meier, Y. Hirayama, R. A. Römer, R. Wiesendanger, and M. Morgenstern, Quantum Hall Transition in Real Space: From Localized to Extended States, Phys. Rev. Lett. **101**, 256802 (2008).

[64] S. Faez, A. Strybulevych, J. H. Page, A. Lagendijk, and B. A. v. Tiggelen, Observation of Multifractality in Anderson Localization of Ultrasound, Phys. Rev. Lett. **103**, 155703 (2009).

[65] A. Richardella, P. Roushan, S. Mack, B. Zhou, D. A. Huse, D. D. Awschalom, and A. Yazdani, Visualizing critical correlations near the metal-insulator transition in $Ga_{1-x}Mn_xAs$, Science **327**, 665 (2010).

[66] A. D. Mirlin, Y. V. Fyodorov, A. Mildenberger, and F. Evers, Exact Relations between Multifractal Exponents at the Anderson Transition, Phys. Rev. Lett. **97**, 046803 (2006).

[67] J. T. Chalker, V. E. Kravtsov, and I. V. Lerner, Spectral rigidity and eigenfunction correlations at the Anderson transition, JETP Lett. **64**, 386 (1996).

[68] R. Klesse and M. Metzler, Spectral Compressibility at the Metal-Insulator Transition of the Quantum Hall Effect, Phys. Rev. Lett. **79**, 721 (1997).

[69] H. U. Baranger and P. A. Mello, Mesoscopic Transport through Chaotic Cavities: A Random *S*-Matrix Theory Approach, Phys. Rev. Lett. **73**, 142 (1994).

[70] D. V. Savin and H.-J. Sommers, Shot noise in chaotic cavities with an arbitrary number of open channels, Phys. Rev. B **73**, 081307(R) (2006).